

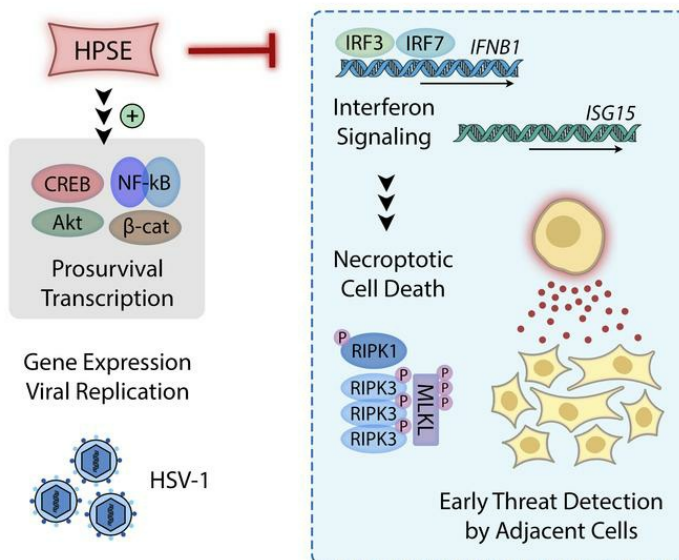
Disruption of innate defense responses by endoglycosidase HPSE promotes cell survival

Alex Agelidis, ... , Patricia W. Finn, Deepak Shukla

JCI Insight. 2021. <https://doi.org/10.1172/jci.insight.144255>.

Research In-Press Preview Cell biology Microbiology

Graphical abstract



Find the latest version:

<https://jci.me/144255/pdf>



1 **Disruption of innate defense responses by**
2 **endoglycosidase HPSE promotes cell survival**

3
4 **Authors**

5 Alex Agelidis^{1,2}, Benjamin A. Turturice^{1,3}, Rahul K. Suryawanshi², Tejabhram Yadavalli², Dinesh
6 Jaishankar^{2,4}, Joshua Ames^{1,2}, James Hopkins^{1,2}, Lulia Koujah^{1,2}, Chandrashekhar D. Patil², Satvik
7 R. Hadigal², Evan J. Kyzar⁵, Anaamika Campeau^{6,7}, Jacob M. Wozniak^{6,7}, David J. Gonzalez^{6,7}, Israel
8 Vlodavsky⁸, Jin-ping Li⁹, David L. Perkins^{10,11}, Patricia W. Finn^{1,3}, Deepak Shukla^{1,2,*}

9
10 **Affiliations**

11 ¹ Department of Microbiology and Immunology, University of Illinois at Chicago, Chicago, IL 60612, USA

12 ² Department of Ophthalmology and Visual Sciences, University of Illinois at Chicago, 1855 West Taylor Street,
13 M/C 648, Chicago IL 60612, USA

14 ³ Division of Pulmonary, Critical Care, Sleep, and Allergy, Department of Medicine, University of Illinois at
15 Chicago, Chicago IL, USA

16 ⁴ Department of Dermatology, Lurie Comprehensive Cancer Center, Northwestern University, Chicago IL, USA

17 ⁵ Department of Psychiatry, University of Illinois at Chicago, Chicago IL, USA

18 ⁶ Department of Pharmacology, University of California, San Diego, La Jolla CA, USA

19 ⁷ Skaggs School of Pharmacy, University of California, San Diego, La Jolla CA, USA

20 ⁸ Technion Integrated Cancer Center (TICC), Rappaport Faculty of Medicine, Technion, Haifa, Israel

21 ⁹ Department of Medical Biochemistry and Microbiology, University of Uppsala, Uppsala, Sweden

22 ¹⁰ Division of Nephrology, Department of Medicine, University of Illinois at Chicago, Chicago IL, USA

23 ¹¹ Department of Surgery, University of Illinois at Chicago, Chicago IL, USA

24 * Correspondence addressed to: dshukla@uic.edu, (312) 996-0908

25
26 **Keywords**

27 Cell death; Defense response; Infection; Inflammation; Innate immunity; Interferon;

28 Necroptosis; Stress response; Transcriptional program

29 **Abstract**

30 The drive to withstand environmental stresses and defend against invasion is a universal trait
31 extant in all forms of life. While numerous canonical signaling cascades have been
32 characterized in detail, it remains unclear how these pathways interface to generate
33 coordinated responses to diverse stimuli. To dissect these connections, we follow heparanase
34 (HPSE), a protein best known for its endoglycosidic activity at the extracellular matrix but
35 recently recognized to drive various forms of late stage disease through unknown mechanisms.
36 Using herpes simplex virus-1 (HSV-1) infection as a model cellular perturbation, we
37 demonstrate that HPSE acts beyond its established enzymatic role to restrict multiple forms of
38 cell-intrinsic defense and facilitate host cell reprogramming by the invading pathogen. We
39 reveal that cells devoid of HPSE are innately resistant to infection and counteract viral takeover
40 through multiple amplified defense mechanisms. With a unique grasp of the fundamental
41 processes of transcriptional regulation and cell death, HPSE represents a potent cellular
42 intersection with broad therapeutic potential.

43 **Introduction**

44 As major constituents of the extracellular matrix of virtually all cells, heparan sulfate and
45 other protein-associated glycans have been well studied as co-receptors for a variety of
46 macromolecules and pathogens. However, very little understanding of their regulatory
47 mechanisms in cell signaling, microbial invasion, and cellular physiology exists. Some recent
48 studies have made startling observations that enzymatic splitting of these sugars at the plasma
49 as well as nuclear membranes may constitute an important regulatory step that promotes
50 inflammation and tissue invasion (1-3). An endoglycosidase, heparanase (HPSE), potentially
51 contributes to pathological inflammatory signaling through its glycosidic action on the
52 extracellular matrix. HPSE is the only known mammalian enzyme capable of splitting polymers
53 of heparan sulfate, and heparan sulfate is the only known enzymatic target of HPSE (1). These
54 chains of heparan sulfate hydrolyzed by HPSE may be present in multiple cellular locations in
55 the context of various proteoglycans (4). Yet HPSE remains a mysterious cellular component, as
56 additional reports of its tendency to appear in the nucleus and regulate gene expression
57 continue to emerge (5, 6). Associations between HPSE and various pathologies, including
58 inflammation and cancer metastasis, have historically been attributed to the protein's cleavage
59 of HS chains at the cell surface and basement membrane (1, 2); however, HPSE may possess
60 unique roles arising independently of its enzymatic active site. Recently our group and others
61 have described yet another important role for HPSE as a driver of microbial pathogenesis. HPSE
62 is now known to be transcriptionally upregulated by several viruses dependent upon heparan
63 sulfate for attachment and entry, and subsequently facilitates egress of newly produced viral
64 particles (7-10). While enzymatic activity of HPSE is believed to enable viral release through
65 splitting of HS residues at the cell surface, it has been reported to also regulate gene expression

66 and trigger proviral signaling through some distinct non-enzymatic activity (11). With a focus on
67 cellular responses to infection, we show here that HPSE acts beyond its known endoglycosidase
68 activity as a potent regulator of the signal transduction phase of cellular defense.

69

70 **Results**

71 **Cells lacking HPSE are intrinsically resistant to HSV-1 infection**

72 Given our unexpected finding that HPSE can directly drive viral pathogenesis (7, 11), we
73 became interested in investigating cellular responses to infection in the absence of HPSE
74 altogether. To our further surprise, HSV-1 infection of Hpse-knockout (KO) mouse embryonic
75 fibroblasts (MEFs) showed a dramatic reduction in virus production, as compared to wildtype
76 MEFs. Virus enters cells at normal levels, but viral replication and protein production are
77 decreased by several orders of magnitude (**Figures 1 and S1**). Hpse-KO cells originally appear
78 capable of immediate early viral gene production, but late gene products are effectively absent
79 (**Figure 1A**). These findings align with previous work from our group and others' showing that
80 active HPSE translocates to the nucleus and influences gene expression through an unknown
81 mechanism (5, 6, 12-14). We therefore adopted an unbiased approach to generate a clearer
82 understanding of how HPSE, or lack thereof, potentially influences gene expression and cell
83 signaling to restrict viral production. RNA-seq analysis constituted the primary exploratory and
84 gene clustering pipeline, while quantitative proteomics analysis of the same samples provided
85 an additional level of functional validation. The transcriptomic landscape of Hpse-deficient cells
86 is markedly altered by ablation of this single locus, with 1,385 genes showing baseline
87 differences in expression (**Figure S1**). Based on gene ontology (GO) analysis of non-infected
88 cells, we observed that Hpse-deficient cells show significant enrichments of genes representing

89 pathways of “defense response to virus” and “activation of immune response”, suggesting that
90 these cells are somehow intrinsically resistant to infection (**Figure 1D**). As an independent
91 confirmation, differential expression analysis of the only existing publicly available dataset of
92 HPSE genetic alteration (GSE34080) yielded strikingly similar results (**Figure S2**). This silencing
93 RNA knockdown of HPSE performed by other investigators in human gastric cancer cells shows
94 significant enrichments of GO terms including “negative regulation of viral genome replication”
95 and “response to type I interferon”, indicating a broad external validity of these newly described
96 HPSE functions.

97

98 **Temporal viromics catalogs transcriptional landscape shifts dependent on HPSE**

99 Hundreds of gene expression changes occur in a viral infection, and as such, viruses
100 represent excellent tools to probe the connections between cellular processes and signaling
101 cascades. To appreciate major regulators of this cellular remodeling and understand how these
102 shifts are influenced by HPSE, we generated clusters of the significantly differentially expressed
103 genes based on temporal expression patterns. Topological clustering using a t-distributed
104 stochastic neighbor embedding (t-SNE) (15) followed by an affinity propagation (APcluster) (16)
105 algorithm produced 13 well-defined clusters (**Figures 2A, S3 and S4**). Further attention to the
106 most heavily induced clusters 9 and 12 revealed that Hpse-deficient cells are hyperactive in
107 antiviral cytokine signaling and cellular defense, while infection of wildtype cells stimulates
108 production of cellular machinery essential for virus assembly (**Figures 2B and 2C**). In fact, cluster
109 12 also contains all viral genes, which are transcribed virtually unimpeded in wildtype cells, while
110 expression of this cluster is stalled in Hpse-KO, concordant with the defense response induction
111 occurring around 12 hpi. We then scanned upstream promoter regions of genes in each cluster

112 using the PASTAA algorithm to identify major transcriptional regulators and correlate with
113 temporal expression patterns (**Figure 2D**). Our finding of highly significant enrichments of
114 multiple interferon regulatory factors (IRFs) and nuclear factor (NF)- κ B as the primary regulators
115 of cluster 9 expression adds further credence to results of the above GO analysis and previous
116 in vitro evidence of an inverse relationship between IRF7 and HPSE gene expression (11).
117 Interestingly, this analysis also designated cAMP responsive element binding protein (CREB) as
118 a major proviral factor, and remarkably, pharmacological blockade of various components of
119 the CREB signaling interface resulted in potent inhibition of virus production in both wildtype
120 MEFs and human epithelial cells. These results further express the value of mechanistic
121 characterization and temporal dissection of gene expression shifts in driving rational drug
122 discovery.

123

124 **HPSE restricts direct antimicrobial activity of type I interferon system**

125 Given the amplified induction of defense and immune-related genes observed in our
126 unbiased analysis of Hpse-deficient cells, we sought to mechanistically define the apparent link
127 between HPSE and innate immune signaling. Subsetting both transcriptomics and proteomics
128 datasets based on the curated “Hallmark Interferon Alpha Response” gene set (MSigDB) shows
129 the striking upregulation of interferon response genes (ISGs) in the absence of HPSE (**Figures**
130 **3A and 3B**). Interferons (IFN) are a highly conserved family of cytokines, with type I IFN (α and
131 β) secreted particularly in response to viral infection and known to exert various antimicrobial
132 functions (17). Using ISG15 as an indicator of signaling activity downstream of type I IFN, Hpse-
133 KO cells are observed to be intrinsically more sensitive to these conserved cytokines. In the
134 absence of HPSE, cells are responsive to levels of purified IFN- β orders of magnitude lower than

135 wildtype cells, with active signaling occurring even without any external stimulus (**Figure 3C**).
136 Interestingly, with a similar size and structure to that of ubiquitin, ISG15 is known to exert
137 antimicrobial activity through direct protein ligation, with downstream consequences including
138 proteasomal degradation and regulation of signal transduction (18). Expression analysis of
139 individual viral proteins by proteomics analysis showed that Hpse-KO cells exhibit a particularly
140 large defect in production of the immediate early protein ICP0, which is known to be essential
141 for HSV-1 replication and assembly (**Figures 3D-3F, S5**) (19, 20). Blocking of the proteasome
142 with MG132 for the last 4 hours of infection somewhat restores ICP0 (110 kDa) and also reveals
143 increased levels of a 66 kDa degradation product previously observed by other investigators
144 (21). Our findings here detail one mechanism of direct antimicrobial action occurring in the
145 absence of HPSE: conjugation of ISG15 to ICP0 correlates with increased proteasomal
146 degradation of this essential viral protein, thus stalling viral replication (**Figure 3G**).

147

148 **Deletion of HPSE protects from cellular infiltration and associated inflammation**

149 To appreciate a broader impact of these findings, we evaluated infection in Hpse-KO
150 mice (22), which showed a significant decrease in virus production by plaque assay after corneal
151 HSV-1 infection (**Figure 4A**). Despite the more modest reduction in virus titers compared to
152 observations in vitro, HSV-1 infected corneas displayed a striking ablation of the typical
153 inflammatory response observed in wildtype mice, evidenced by loss of CD45⁺ Gr-1⁺ neutrophil
154 and monocyte infiltration at 7 and 14 dpi (**Figures 4B-4E**). Absolute cell infiltration counts and
155 flow cytometry gating strategy are displayed in **Figure S6**. In accordance with previous studies
156 of the murine keratitis model, we observed that viral titers peak in both genotypes at 2 dpi, while
157 substantial cellular infiltration to the cornea does not occur before 5 dpi, and was thus measured

158 at 7 and 14 dpi (23, 24). Infected Hpse-KO mice also showed a significant increase in corneal IFN-
159 β mRNA, in line with our in vitro findings (**Figure 4F**). A baseline difference in IFN- β transcripts
160 was not observed in corneal epithelium, possibly due to additional compensatory changes that
161 occurred in the process of cell differentiation in vivo. Furthermore, ocular application of
162 monoclonal antibodies against interferon- α receptor (α -IFNAR) resulted in a significant
163 restoration of virus production and infiltrative phenotypes, including increased cellularity of
164 draining lymph nodes and marked corneal opacity (**Figures 4G-4J**). These results may suggest
165 that resident corneal cells lacking HPSE are intrinsically more effective in neutralizing the virus
166 rather than inciting the nonspecific granulocytic infiltration known to be pathogenic in herpes
167 keratitis. Collectively, these findings demonstrate that HPSE restriction of the type I IFN system
168 is a potent immunomodulatory mechanism, and upregulation of HPSE may be a common
169 microbial strategy for evasion of innate immune responses.

170

171 **Necroptosis is an interferon-induced stress response limited by HPSE**

172 Another initial observation from our studies was that Hpse-deficient cells appear to
173 possess the intrinsic ability to contain infection before considerable viral spread can occur. This
174 finding suggests that in the absence of HPSE, infected cells undergo some form of programmed
175 cell death to shut down virus production. Indeed, Hpse-KO cells are more prone to virus-induced
176 cell death, and possibly exhibit increased levels of basal cell death, measured as increased PI
177 uptake by flow cytometry (**Figure 5A**). Although effective viral production is markedly hindered
178 in the absence of HPSE, small clusters of rounded and dead cells similar to plaques are frequently
179 observed after infection (**Figure 5B**). Interestingly, recent studies have suggested that
180 necroptosis, or programmed necrosis, is a major mechanism of virus-induced cell death, which

181 may provide some level of protection to the infected host (25-27). Moreover, type I IFNs are
182 known drivers of necroptosis in response to various cellular stresses including viral infection (17).
183 Western blot analysis of an infection time course showed a pronounced increased abundance
184 of a key protein required for induction of necroptosis, receptor-interacting serine/threonine-
185 protein kinase 3 (RIPK3), in the absence of HPSE (**Figure 5C**). Increased abundance of mixed
186 lineage kinase domain-like pseudokinase (MLKL) was also observed, while no apparent
187 difference in other key proteins including RIPK1 and Caspase 8 was noted. Phosphorylated MLKL
188 (p-MLKL), an indication of necroptosis activation, was found to be elevated at baseline in Hpse-
189 KO cells, and induced as early as 12 hpi, whereas wildtype cells did not show any considerable
190 level of p-MLKL until 36 hpi. This finding suggests that HPSE-deficient cells undergo some basal
191 level of necroptosis and that these cells are more sensitive to necroptosis induction by
192 exogenous stimuli. Using inhibitors of the type I IFN system (α -IFNAR) and necroptosis (Nec-1)
193 in combination, infection in Hpse-KO cells is nearly restored to wildtype levels (**Figures 5D-5F**).
194 Evaluation of inhibitors of apoptosis (ZVAD) and necroptosis (Nec-1) shows that HPSE
195 preferentially limits necroptosis to promote cell survival and thus virus production. As many
196 viruses including HSV-1 are known to block cell death to promote viral production and spread,
197 clearance of infected cells through HPSE inhibition may hold great therapeutic potential.

198

199 **Bioinformatics-guided analysis of transcription factor activation in HSV-1 infection** 200 **identifies potent antiviral compounds**

201 While gaining an understanding of the major antiviral pathways active in Hpse-KO cells,
202 we remained interested in targeting proviral networks activated upon infection of wildtype
203 cells. Analysis of divergent responses between these two cell types provided the initial clues

204 that cAMP response element-binding protein (CREB) and β -catenin are drivers of proviral
205 signaling. CREB was identified as a key driver of cluster 12 expression through transcription
206 factor binding site analysis of RNA-seq data (**Figure 2**), while β -catenin was detected as a major
207 hub gene from proteomics analysis of differentially expressed proteins. In light of these results
208 and the above findings that HPSE inhibits functional interferon signaling, we pursued further
209 experiments under the following rationale (**Figure 6A**). Years of published work informed us
210 that interferon regulatory factors, including IRF3, IRF7 and IRF9, bind to CREB-binding protein
211 (CBP) and histone acetyltransferase p300 to drive optimal transcription of type I IFN and
212 downstream IFN-stimulated genes (28, 29). Thus, these IRFs in effect compete with CREB and
213 other transcription factors for CBP/p300 occupancy and binding to respective cAMP response
214 elements (CRE) or interferon-sensitive response elements (ISRE). We also found that an inverse
215 association exists between the CREB and IFN in that inhibitors of the CREB-CBP-p300 system
216 resulted in induction of IFN- β in human cells (**Figure S7A**). Conversely, exogenous IFN- β led to
217 a decrease in total CREB protein levels in cells lacking HPSE (**Figure S7B**). Additionally, we
218 focused some attention to EGR1, a transcription factor shown by multiple studies to drive HPSE
219 upregulation (30, 31), and act as a supporter of IFN signaling (32, 33). Interestingly, various
220 studies have also drawn connections of EGR1 with necroptosis, CREB signaling and viral
221 infection (34-37).

222 Indeed, western blot and immunofluorescence microscopy confirmed that activation of
223 the CREB and β -catenin systems occurs upon infection of wildtype MEFs, while Hpse-KO cells
224 do not display these changes (**Figures 6B-6D**). CREB is upregulated in wildtype cells starting at
225 12 hpi, while this response is absent in Hpse-KO. Likewise, phosphorylation of β -catenin at the
226 S33/S37/T41 sites, indicative of inactive β -catenin (38), is decreased across infection timepoints,

227 while this phosphorylation is increased in Hpse-KO. A similar trend is observed for p-GSK-3 β ,
228 which when phosphorylated at the S9 site is known to result in β -catenin activation through
229 double inhibition (38). We also noted profound differences in EGR1 abundance and localization
230 dependent on HPSE expression (**Figure 6E**). Given these supportive findings, we opted to treat
231 cells with inhibitors targeting the CREB or β -catenin systems by therapeutic application at
232 various concentrations at 2 hpi after viral entry had occurred. The identities and mechanisms
233 of these compounds are shown in **Figure 6F**. Initial testing was performed in wildtype MEFs;
234 upon detection of antiviral efficacy we transitioned to human corneal epithelial (HCE) cells, a
235 model cell line for HSV-1 infection. Images from GFP-HSV-1 and viral titers from HCE cell culture
236 supernatants collected at 24 hpi demonstrate antiviral efficacy of these compounds (**Figures**
237 **6F and 6G**). By merging our unbiased temporal analysis with various molecular manipulations,
238 we show that through activation of these two host factors with broad control over cellular
239 physiology, HSV-1 generates an environment conducive to its own propagation and
240 persistence (**Figure 6H**).

241

242 **Discussion**

243 With this multidisciplinary exploration of various cellular responses to stress, we
244 demonstrate how HPSE serves as a key intersection between the detection and effector phases
245 of signal transduction. Using a genome-wide analysis of HPSE-deficient cells, we aimed to
246 define the factors and related pathways that make these cells naturally resistant to infection.
247 Our results show that considerable differences in baseline gene expression exist in these cells
248 compared to wildtype, possibly due to compensatory mechanisms that have emerged
249 throughout embryonic development in the absence of HPSE. Viral infection triggers extensive

250 remodeling of host cellular processes. By understanding the connections between these
251 processes, we can infer their reliance on HPSE in the case of wildtype cells. The temporal
252 viromics methods employed here reliably clustered differentially expressed genes and
253 identified transcription factors regulating major shifts in cellular programs over time. This
254 unique analysis thus draws an indirect connection between HPSE and multiple important
255 drivers of cellular proliferation and defense. In agreement with our previous work, we show by
256 transcription factor binding site analysis that IRFs and NF- κ B are major drivers of the defense
257 response gene cluster heavily upregulated with infection in Hpse-KO cells. We further dissect
258 this relationship in vitro and in vivo by rescuing virus production in Hpse-KO with inhibition of
259 the IFN and necroptosis systems. Of note, a majority of studies have used multiplicities of
260 infection (MOI) of HSV-1 in the 1 to 100 range for induction of IFN signaling in MEFs. In this
261 study, we focused on an MOI of 0.1, more commensurate to productive infection occurring in
262 vivo. Our results highlight the increased sensitivity of Hpse-KO cells to induction of the type I
263 IFN response upon low grade viral infection. Future studies will aim to more precisely define
264 the nature of the first-order interactions between HPSE and effectors as these remain almost
265 entirely unknown. Given the regulatory relationship that exists between EGR1 and HPSE (30,
266 31), we suspect that in the absence of HPSE expression, EGR1 upregulation upon infection
267 remains unchecked, and that this uncontrolled EGR1 level results in hyperactivation of the type
268 I IFN system. Further mechanistic studies will be required to dissect the antiviral mechanisms
269 displayed by EGR1. Moving forward, high-throughput analyses with even greater temporal
270 resolution will continue to unearth unique connections not previously imagined, yet the
271 importance of molecular validation by conventional methods will remain. Additionally, these
272 newly reported activities of HPSE can help explain the documented roles of HPSE in cancer

273 progression. Numerous malignancies have been shown to increase expression of HPSE,
274 understood to drive late stage metastatic potential (1, 2). Recent studies have also shown that
275 the type I interferon system has control over cancer spread as depletion of IRF7 increases
276 metastatic burden in mice and humans (39, 40).

277 In search for the mechanism of cell death occurring preferentially in cells lacking HPSE,
278 we considered contributions from multiple cellular systems including reactive oxygen species
279 (ROS), mitophagy, inflammasome activation, pyroptosis and apoptosis. With a focus on ROS
280 production, we observed no difference between genotypes or with infection, however ROS
281 scavenging compounds like N-acetylcysteine and urolithin A were indeed found to decrease
282 ROS production as expected (**Figure S8**). Induction of mitophagy with urolithin A does appear
283 to have an alleviating effect on cell death in Hpse-KO cells as observed by propidium iodide
284 uptake. Gene subset analysis of our transcriptomics and proteomics data suggested that some
285 differences exist in mitophagy baseline levels and induction dependent on HPSE, however no
286 clear expression pattern or gene candidate stood out at this time, and this will be the subject
287 of ongoing studies. On the other hand, p-MLKL appears much earlier in infection in Hpse-KO
288 cells, suggesting this enhanced initial sensitivity is important in the marked difference in the
289 subsequent host cell response. A more rapid induction of p-MLKL and substantial rescue of
290 virus production with Nec-1 occurring in HPSE-deficient cells point toward necroptosis as a
291 major form of cell death occurring in the absence of HPSE. As ZVAD acts by blocking the active
292 site of caspases, the fact that virus production is partially restored with Nec-1 and not ZVAD
293 suggests a caspase-independent form of cell death is dominant. Further, western blot analysis
294 showed negligible differences in inflammasome and pyroptosis activation (noted by IL-1 β ,
295 caspase-1 and gasdermin D cleavage) and only minor levels of apoptosis activation occurring

296 at later timepoints (noted by caspase-3 and caspase-8 cleavage) (**Figure S9**). Additionally, no
297 apparent difference in accumulation of ubiquitinated proteins was observed between the two
298 cell types. Full length western blots for all figures are presented in **Figure S10**.

299 We also identify two novel proviral transcriptional regulatory factors CREB and β -
300 catenin that are activated in wildtype cells, and demonstrate that their pharmacological
301 inhibition in human cells is a highly effective antiviral strategy resulting from this analysis. We
302 show that through activation of these two factors with broad control over cellular physiology,
303 the virus generates an environment conducive to its own success. CREB is a transcription factor
304 well studied in the neuroscience field, but with little mention in studies of microbial
305 pathogenesis. It is known to be activated by protein kinases upon second messenger signaling
306 and bound by coactivators CREB-binding protein (CBP) and p300 for its binding to DNA
307 sequences (41). CREB has also been documented to interact with various signaling molecules
308 including signal transducer of and activator of transcription (STAT1) and NF- κ B, indicating
309 potential ramifications for generation of immune responses (42, 43). Likewise, β -catenin is a
310 well-studied regulator of transcription and cell adhesion overexpressed in several cancers,
311 which is part of a multi-protein destruction complex. Numerous protein interactions and
312 regulators of β -catenin have been characterized, with one known transcriptional co-activator
313 being CBP for DNA binding. The association between this prosurvival factor and infection
314 remains understudied as only a small number of studies exist linking HSV-1 or other viral
315 infection to β -catenin activation (44-46). In this study, we show that multiple commercially
316 available compounds targeting CREB and β -catenin systems demonstrate antiviral efficacy
317 against HSV-1 and display an inverse relationship with type I IFN signaling. While some degree
318 of cellular toxicity was noted at higher concentrations, all compounds tested displayed antiviral

319 efficacy, with PRI-724 showing the most appealing profile of antiviral activity over toxicity.
320 Interestingly, this compound is currently in clinical trials for hepatitis C virus hepatocellular
321 carcinoma and other cancers (47), and along with the other compounds analyzed here may
322 prove a promising antiviral candidate. Our findings showcase a success of mechanism-based
323 rational drug design informed by multi-perspective analysis merging systems and molecular
324 investigation.

325

326 **Materials and Methods**

327 **Mice**

328 6-10-week-old male and female mice on C57/B6 background (wildtype or Hpse-deficient) were
329 used for all experiments. Anaesthetized mouse corneas were scarified in a 3x3 grid using a 30-
330 gauge needle, and infected as previously described (11). All images of the corneal surface were
331 acquired with SteREO Discovery.V20 stereoscope (Zeiss, Germany). For IFNAR blockade
332 experiment, 5 μ L α -IFNAR monoclonal antibody (Leinco I-401) was applied topically to corneas
333 of mice once 24 h prior to infection and then daily for 3 days post infection. Ocular infection was
334 performed as described above and mice were sacrificed at 45 dpi for tissue analysis.

335

336 **Cell lines and virus strains**

337 Human corneal epithelial (HCE) cell line (RCB1834 HCE-T) was obtained from Kozaburo Hayashi
338 (National Eye Institute, Bethesda, MD) and was cultured in MEM (Life Technologies, Carlsbad,
339 CA) with 10% fetal bovine serum (FBS) (Life Technologies) and 1% penicillin/streptomycin (Life
340 Technologies). Confirmation of identity of HCE cell line was done by short tandem repeat
341 analysis. Vero cell line for virus preparation and plaque assay was provided by Dr. Patricia G.

342 Spear (Northwestern University, Chicago, IL) and cultured in DMEM (Life Technologies) with 10%
343 FBS and 1% penicillin/streptomycin. Wildtype and heparanase-knockout mouse embryonic
344 fibroblasts (WT and Hpse-KO MEFs) were provided by Dr. Israel Vlodavsky (Rappaport Institute,
345 Haifa, Israel) (22). All cells were maintained in a Heracell VIOS 160i CO2 incubator (Thermo
346 Scientific) and have been confirmed negative for mycoplasma contamination. Virus strains used
347 in these studies, HSV-1 (KOS-WT) (48), GFP-HSV-1 (K26-GFP) (48), HSV-1 (gL86) (49), McKrae and
348 pseudorabies virus (PRV) (50) were provided by Dr. Patricia G. Spear (Northwestern University,
349 Chicago, IL). Dual color ICP0_p-GFP/gC_p-RFP was a gift of Dr. Paul Kinchington (University of
350 Pittsburgh). HSV-1 infections were performed with strain KOS at MOI=0.1 unless otherwise
351 specified. All virus stocks were propagated in Vero cells and stored at -80°C.

352

353 **Antibodies and plasmids**

354 The following antibodies were used for western blot studies: from Cell Signaling Technology, at
355 dilution 1:1000 – CREB (9197), CBP (7389), p300 (86377), β -catenin (8480), phospho- β -catenin
356 (9561), EGR1 (4154), RIPK1 (3493), RIPK3 (95702), MLKL (37705), phospho-MLKL (37333), CASP1
357 (24232), cleaved CASP1 (89332), CASP3 (14220), cleaved CASP3 (9664), CASP8 (4927), IL-1 β
358 (12507), cleaved IL-1 β (63124), gasdermin D (39754), cleaved gasdermin D (10137); from Santa
359 Cruz Biotechnology, at dilution 1:250 – GSK-3 β (sc-7291), phospho-GSK-3 β (sc-373800), ICP0 (sc-
360 53070), ICP4 (sc-69809), ICP27 (sc-69806), ISG15 (sc-166755), ubiquitin (sc-8017); from
361 Proteintech, at dilution 1:1000 – GAPDH (10494); from Abcam, at dilution 1:10,000 – gB (ab6505).
362 The following antibodies were used for immunofluorescence microscopy studies: from Cell
363 Signaling Technology, at dilution 1:100 – CREB (9197), EGR1 (4154). HPSE expression constructs
364 including Myc-GS3 plasmid were provided by Dr. Israel Vlodavsky (Rappaport Institute, Haifa,

365 Israel) (51). Lipofectamine-2000 transfection reagent (Life Technologies, 11668019) was used for
366 all in vitro overexpression experiments, according to the manufacturer's specifications.

367

368 **Chemical reagents**

369 Anti-mouse interferon alpha receptor 1 (α -IFNAR) was purchased from Leinco (St. Louis, MO) and
370 was used at concentrations ranging from 0.1 μ g/mL to 10 μ g/mL, as indicated (I-401, clone
371 MAR1-5A3). Mouse isotype control antibody (mouse IgG1, Cell Signaling 5415) was used as a
372 negative control for this antibody where applicable. Necrostatin-1 (Nec-1) was used to inhibit
373 necroptosis and was purchased from Selleckchem (Houston, TX) and used at 50 μ M, unless
374 otherwise specified (S8037). Pan-caspase inhibitor Z-VAD-FMK was used at 10 μ M to block
375 apoptosis and was purchased from Selleckchem (S7023). MG132 was used at 10 μ M to inhibit
376 proteasomal degradation of proteins and was purchased from Selleckchem (S2619).
377 Pharmacological inhibitors of the CREB/CBP/ β -catenin system were purchased from
378 Selleckchem (PRI-724, S8262; KG-501, S8409; C646, S7152) and Tocris Biosciences (666-15, 5661).
379 Purified mouse interferon- β was purchased from PBL Assay Science (Piscataway, NJ) (12405-1).
380 Urolithin A was purchased from Selleckchem (S5312) and used as an inducer of mitophagy. N-
381 acetylcysteine was purchased from Selleckchem (S1623) and used as an antioxidant.

382

383 **Western blot**

384 Cellular proteins were extracted using the following lysis buffer: 150 mM NaCl, 50 mM Tris-HCl
385 pH 7.4, 10% glycerol, 1% NP-40, 10 mM sodium fluoride, 1 mM sodium orthovanadate, 10 mM
386 N-ethylmaleimide, and Halt Protease Inhibitor Cocktail (Thermo Scientific). Lysis was performed
387 on ice with agitation for 30 min, followed by 30 min centrifugation at 13,000 rpm. Clarified

388 lysates were then denatured at 95°C for 8 min in the presence of 4X LDS sample loading buffer
389 (Life Technologies) and 5% beta-mercaptoethanol (Bio-Rad, Hercules, CA) and separated by
390 SDS-PAGE with NuPAGE 4-12% Bis-Tris 1.5 mm 15-well gels (Thermo Scientific). Proteins were
391 then transferred to nitrocellulose using iBlot2 system (Thermo Scientific) and membranes were
392 blocked in 5% milk/TBS-T for 1 h, followed by incubation with primary antibody overnight. After
393 washes and incubation with respective horseradish peroxidase-conjugated secondary
394 antibodies (Jackson ImmunoResearch Peroxidase AffiniPure goat anti-mouse IgG (H+L), 115-
395 035-146 at 1:10,000 or Peroxidase AffiniPure goat anti-rabbit IgG (H+L), 111-035-003 at 1:20,000)
396 for 1 h, protein bands were visualized using SuperSignal West Femto substrate (Thermo
397 Scientific) with Image-Quant LAS 4000 biomolecular imager (GE Healthcare Life Sciences,
398 Pittsburgh, PA).

399

400 **Immunopurification**

401 Immunopurification (IP) of proteins was performed using HCE cells cultured in 15 cm dishes.
402 Cells were collected after specified times of infection and/or treatment, washed with PBS,
403 scraped in cold PBS on ice and transferred to conical tubes. Cells were centrifuged at 1200 rpm
404 for 5 min, then cellular proteins were extracted with lysis buffer: 150 mM NaCl, 50 mM Tris-HCl
405 pH 7.4, 10% glycerol, 1% NP-40, 10 mM sodium fluoride, 1 mM sodium orthovanadate, 10 mM
406 N-ethylmaleimide, and Halt Protease Inhibitor Cocktail (Thermo Scientific). After 30 min of lysis
407 with agitation at 4°C, lysates were centrifuged at 13,000 rpm for 30 min to pellet insoluble
408 cellular debris. IP antibody, ICP0 (Santa Cruz, sc-53070) or isotype control (mouse IgG1, Cell
409 Signaling 5415) were then added to clarified lysates and rotated for 16 h at 4°C. Protein A/G
410 Dynabeads (Thermo Scientific, 88802) were added and samples were rotated for 1 h at 4°C. Four

411 washes with magnetic separation were performed with lysis buffer. Beads were finally
412 resuspended in LDS buffer with 5% beta-mercaptoethanol, denatured at 95°C for 8 min, and
413 SDS-PAGE was performed.

414

415 **Quantitative polymerase chain reaction**

416 RNA was extracted from cultured cells using TRIzol (Thermo Scientific, 15596018), following the
417 manufacturer's protocol, and complementary DNA was produced using High Capacity cDNA
418 Reverse Transcription kit (Life Technologies). Where applicable, corneal tissues were extracted
419 from mice and incubated in 50 µL of 2 mg/mL collagenase D (Sigma C0130) in PBS for 1 h at
420 37°C. Tissues were then triturated with a pipet tip, resuspended in TRIzol and extraction of RNA
421 and cDNA were performed as above. Real-time quantitative polymerase chain reaction (qPCR)
422 was performed using Fast SYBR Green Master Mix (Life Technologies) on QuantStudio 7 Flex
423 system (Life Technologies). To quantify viral genomes, infected cell pellets were resuspended in
424 500 µL virion buffer: 8 mg/mL Tris-HCl, 1% SDS, 10 mM EDTA supplemented with 1 µL proteinase
425 K (Thermo Scientific EO0491) and incubated at 55°C for 16 h. Viral DNA was then extracted by
426 adding 500 µL of Ultrapure phenol chloroform isoamyl alcohol mix (Thermo Scientific 15593-
427 031), according to the manufacturer's specifications. The gD-specific primers listed below were
428 then used to quantify HSV-1 genomes.

429

430 The following mouse-specific primers were used in this study:

431 IFN-β Fwd 5'-TGTCCTCAACTGCTCTCCAC-3', Rev 5'-CATCCAGGCGTAGCTGTTGT-3'

432 ISG15 Fwd 5'-AGCAATGGCCTGGGACCTAAAG-3', Rev 5'-CCGGCACACCAATCTTCTGG-3'

433 β-actin Fwd 5'-GACGGCCAGGTCATCACTATTG-3', Rev 5'-AGGAAGGCTGGAAAAGAGCC-3'

434

435 The following HSV-1-specific primers were used in this study:

436 gD Fwd 5'-GTGTGACACTATCGTCCATAC-3', Rev 5'-ATGACCGAACAACTCCCTAAC-3'

437 ICP0 Fwd 5'-ACAGACCCCCAACACCTACA-3', Rev 5'-GGGCGTGTCTCTGTGTATGA-3'

438

439 **Plaque assay**

440 Cell monolayers were inoculated for 2 h in Opti-MEM (Thermo Scientific) with incubation at 37°C,
441 5% CO₂, after which viral suspension was aspirated and replaced with complete media for
442 remaining infection time course. To quantify extracellular virus, culture supernatants were
443 collected, centrifuged at 13,000 rpm for 1 min, serially diluted in Opti-MEM, and overlaid on
444 confluent monolayers of Vero cells in 24-well plates. After 2 h incubation, plaque inocula were
445 aspirated, and cells were incubated with complete DMEM containing 0.5% methylcellulose
446 (Fisher Scientific) for 48 to 72 h. Medium was then aspirated, cells were fixed with 100%
447 methanol and finally stained with crystal violet solution to visualize plaques.

448

449 **Viral β-galactosidase entry assay**

450 Cell monolayers were inoculated with recombinant HSV-1 strain gL86, in which a portion of the
451 gL gene was replaced with the lacZ gene encoding β-galactosidase. Only upon successful entry
452 and expression of the viral genome is the β-galactosidase enzyme produced, and this virus is
453 only capable of one round of viral replication; newly produced virions will not be capable of
454 downstream infection. At 6 h post infection, cells were washed once with PBS and incubated at
455 37°C for 1 h with ONPG solution (3 mg/mL (Fisher Scientific, 34055) + 0.05% NP-40) and

456 colorimetric substrate was detected at 410 nm using a microplate reader (Tecan GENious Pro,
457 Mannedorf, Switzerland).

458

459 **Reactive oxygen species detection assay**

460 Wildtype and Hpse-KO MEFs were incubated with specified treatments for 24 h and cell culture
461 supernatants were collected. ECL substrate SuperSignal West Pico (Pierce 34080) reagents A and
462 B were mixed in an equal ratio and 50 μ L was added to 100 μ L of cell culture supernatant in flat-
463 bottom 96-well plates. Photon counts were determined by Biotek Synergy H1 microplate reader.

464

465 **Immunofluorescence microscopy**

466 HCE cells or wildtype and Hpse-KO MEFs were cultured in glass bottom dishes (MatTek
467 Corporation, Ashland, MA) or 8-well μ -slides (iBidi, Madison, WI). Cells were fixed in 4%
468 paraformaldehyde for 10 min and permeabilized with 0.1% Triton-X for 10 min at room
469 temperature for intracellular labeling. This was followed by incubation with primary antibody
470 for 1 h at room temperature. When a secondary antibody was needed, cells were incubated with
471 respective FITC- or Alexa Fluor 647-conjugated secondary antibody (Sigma-Aldrich F9137 or
472 Thermo Scientific A21244) at a dilution of 1:100 for 1 h at room temperature. NucBlue Live
473 ReadyProbes Hoechst stain (Thermo Scientific R37605) was included with secondary antibody
474 stains when applicable, according to manufacturer's specifications. Samples were examined
475 under LSM 710 confocal microscope (Zeiss) using a 63X oil immersion objective. For cell surface
476 staining, cells were incubated with respective antibodies prior to fixation with
477 paraformaldehyde for imaging. Fluorescence intensity of images was calculated using ZEN
478 software.

479

480 **Live cell imaging**

481 Wildtype and Hpse-KO MEFs were cultured in 24-well plates and infected with HSV-1 dual color
482 fluorescent virus expressing GFP driven by ICP0 promoter and RFP driven by gC promoter. At 2
483 hpi, inoculation media was replaced with complete DMEM, and cells were placed in the
484 incubation chamber of Zeiss spinning disk live-cell imaging system, which maintains conditions
485 of 37°C and 5% CO₂. Images were captured on RFP, GFP, and brightfield at an interval of 30 min
486 for 36 h, and analyzed with ZEN software.

487

488 **Propidium iodide cell death assay**

489 Specified treatments were incubated with wildtype and Hpse-KO MEFs at 2 hpi in complete
490 DMEM including propidium iodide (2 mg/mL) and Hoechst nucleic acid stain. At 24 hpi, Biotek
491 Lionheart FX system was used to detect fluorescence intensity on PI, DAPI and brightfield
492 channels. Gen5 software was used to quantify positive events over 4 images per sample, and
493 propidium iodide index was calculated as the quotient of PI+ events over DAPI+ events.

494

495 **Flow cytometry**

496 Corneas were extracted from mice after euthanasia and treated with 2 mg/mL collagenase D
497 (Sigma C0130) for 1 h at 37°C and triturated with a pipet tip. Cell suspensions were filtered
498 through a 70 µm mesh, resuspended in FACS buffer (PBS + 5% FBS), and counted by
499 hemocytometer. 10⁶ cells from each sample were aliquoted into U-bottom 96-well plates for
500 subsequent staining. F_c-receptors were blocked using TruStain fcX (101319, Biolegend, San
501 Diego, CA), and the following fluorophore-conjugated primary antibodies from Biolegend were

502 used for cell surface staining: FITC anti-mouse CD45 (103107) and APC anti-mouse Ly-6G/Ly-6C
503 (Gr-1) (108411). Cells were immunolabeled, washed, and analyzed with Accuri C6 Plus flow
504 cytometer (BD Biosciences). For flow cytometric quantification of cell death by PI uptake, cells
505 were either infected with HSV-1 KOS (MOI=0.1, MOI=1) or mock treated for 24 h in medium
506 containing PI. At the termination of cellular incubations, cells were collected on ice, washed
507 twice with FACS buffer and analyzed with Accuri C6 Plus flow cytometer. BD Accuri C6 Plus
508 software and Treestar FlowJo v10.0.7 were used for all flow cytometry data analysis.

509

510 **Mouse tissue sectioning and staining**

511 For hematoxylin and eosin staining, mice whole eyes were extracted after euthanasia, washed
512 in PBS, embedded in Tissue-Tek OCT compound (Sakura Finetek), frozen on dry ice and stored
513 at -80°C. 10 µm sections were cut and adhered to Superfrost Plus glass slides (Fisher Scientific)
514 using Cryostar NX50 microtome (Thermo Scientific), air dried at room temperature for 10 min
515 and then fixed in ice-cold acetone for 5 min. Slides were then incubated in the following series:
516 2 min running water, 1 min Mayer's hemalum solution (Merck HX73030749), 2 min running
517 water, 2 min 70% ethanol, 1 min 100% ethanol, 1 min eosin Y solution with phloxine (Sigma
518 HT110316), 2 min 70% ethanol, 1 min 100% ethanol, 1 min xylene, and finally mounted and
519 cover slipped with permount. Slides were then imaged using Zeiss Axioskop 2 Plus microscope.

520

521 **RNA sequencing**

522 Wildtype and Hpse-KO MEFs were cultured in biological triplicates in 10 cm dishes with HSV-1
523 infection using strain KOS (MOI=0.1) at timepoints of 0, 12, 24 and 36 hpi for a total of 24 samples.
524 At specified timepoints, cells were washed once in PBS, and collected by scraping on ice. 10^6

525 cells from each dish were used for RNA-seq workflow, and remaining 4×10^6 cells were used for
526 qProteomics; the two analyses were performed on the same sets of cells. Cell pellets were
527 suspended in RNAlater (Thermo Scientific, AM7020) and stored at -80°C until further processing.
528 RNeasy Mini kit (Qiagen, 74104) was used to extract RNA, and DNA libraries for sequencing were
529 constructed using Nextera XT DNA Library Prep kit (FC-131-1024, Illumina, San Diego, CA). The
530 24 prepared libraries were pooled and submitted to Michigan State University Genomics Facility,
531 where they were quality checked using Qubit dsDNA HS, Agilent Bioanalyzer DNA 1000 and
532 Kapa Illumina Library Quantification qPCR assays. The pool of libraries was loaded onto one lane
533 of an Illumina HiSeq 4000 flow cell and sequencing was performed in a 2 x 150 bp paired end
534 format using HiSeq 4000 SBS reagents (Illumina) and approximately 312 million acceptable
535 quality reads were achieved. Base calling was done by Illumina Real Time Analysis v2.7.7 and
536 output was demultiplexed and converted to FastQ format with Illumina Bcl2fastq v2.19.1.
537 Assembly and alignment to *Mus musculus* (GRCm38.p6) and HSV-1 (JQ673480.1) genomes was
538 performed with CLC Genomics Workbench. Subsequent analyses were performed in *R* v3.5.
539 Differential expression analysis and normalization was performed with DESeq2, with design = ~
540 Genotype + Time.point + Genotype:Time.point and reduced model = ~ Genotype + Time.point,
541 using likelihood relatedness test. Clustering of significantly differentially expressed genes (alpha
542 = 0.01) was performed with Rtsne (15) and APcluster (16) based on temporal expression pattern.
543 Transcription factor binding site enrichment analysis was performed using the PASTAA
544 algorithm (52). Time series splines were generated with MetaLonDA (53). Gene ontology analysis
545 was performed with ClueGO v2.5.2 (54) within Cytoscape v3.6.1 and ClusterProfiler v3.10.0 (55)
546 in *R*.

547

548 **Mass spectrometry-based proteomic sample preparation**

549 Proteomic samples were processed as previously described with minor alterations (56). Cell
550 pellets from HSV-1 infection time course were resuspended in 500 μ L lysis buffer (75 mM NaCl,
551 3% SDS, 1 mM NaF, 1 mM β -glycerophosphate, 1 mM sodium orthovanadate, 10mM sodium
552 pyrophosphate, 1 mM PMSF, 50 mM HEPES pH 8.5, and 1X Roche Complete EDTA-free protease
553 inhibitor cocktail, followed by addition of 500 μ L solution of 8 M urea + 50 mM HEPES pH 8.5,
554 and solubilized by probe sonication. Samples were next subjected to reduction of disulfide
555 bonds in 5 mM DTT for 30 min at 56°C. Free disulfide bonds were then alkylated for 20 min in
556 the dark via the addition of iodoacetamide to a final concentration of 15 mM, followed by
557 addition of the original volume of DTT and 15 min incubation in the dark. One quarter volume
558 of trichloroacetic acid was then added to precipitate proteins. Samples were incubated on ice
559 for 10 min, then centrifuged for 5 min at 18,000 x g at 4°C. The supernatant was removed and
560 protein was washed twice via addition of ice-cold acetone, followed by centrifugation at 18,000
561 x g for 2 min between each wash. Pellets were dried and resuspended in a solution of 1 M urea
562 + 50 mM HEPES pH 8.5 for digestion, performed in two steps. First, samples were incubated
563 overnight at room temperature on a shaker in presence of 3 μ g LysC Endopeptidase (VWR). Next,
564 samples were incubated for 6 h at 37°C with 3 μ g Sequencing Grade Modified Trypsin
565 (Promega). Digestion was terminated via addition of 20 μ L trifluoroacetic acid (TFA). Samples
566 were subjected to centrifugation at 18,000 x g for 5 min to pellet insoluble debris, and
567 supernatants were desalted using C18 resin columns (Waters) and samples were dried under
568 vacuum. Extracted peptides were resuspended in a solution of 50% acetonitrile + 5% formic acid
569 (FA) and quantified using a Quantitative Colorimetric Peptide Assay (Pierce), as recommended

570 by the manufacturer. 50 µg of each sample was separated for subsequent sample preparation.
571 A pooled “bridge channel” was made containing equal amounts from each sample, and two 50
572 µg aliquots were separated for inclusion in subsequent sample preparation steps. 50 µg aliquots
573 were dried under vacuum. 50 µg aliquots were next labeled using tandem mass tags (TMT)
574 (Thermo Scientific, 90309). Dried peptides were resuspended in a solution of 30% dry
575 acetonitrile (ACN) + 200 mM HEPES pH 8.5. Label assignment was performed so that each
576 biological replicate was represented within each 10-plex, and such that no two replicates were
577 assigned to the same label, except for the bridge channel internal standards. 8 µL of 20 µg/µL
578 TMT solution was added to the appropriate assigned sample, and the labeling reaction was
579 allowed to proceed for 1 h at room temperature. Reaction quenching was performed via
580 addition of 9 µL 5% hydroxylamine at room temperature for 15 min. 50 µL 1% TFA was added to
581 each sample, and samples within each 10-plex experiment were multiplexed, desalted and
582 vacuum dried as described above. 10-plexes were fractionated using reverse phase high pH
583 liquid chromatography. Samples were resuspended in 110 µL 5% ACN + 5% FA. Fractionation
584 was performed on an Ultimate 3000 HPLC with 4.6 mm x 250 mm C18 column. Samples were
585 separated on a 1 h solvent gradient ranging from 5% to 90% ACN + 10 mM ammonium
586 bicarbonate. Fractions were pooled as previously described and dried under vacuum (57).
587 Alternating pooled samples were used for subsequent analysis, except for the tenth pooled
588 fraction, where its complement was used.

589

590 **Mass spectrometry-based proteomic analysis**

591 Dried fractions were resuspended in 8 μ L 5% ACN + 5% FA and analyzed on an Orbitrap Fusion
592 with in-line Easy Nano-LC 1000 (Thermo Scientific). Fractions were run as 3 h gradients
593 progressing from 3% ACN + 0.125% FA to 100% ACN + 0.125% FA. Fractions were loaded onto
594 an in-house packed column of 0.5 cm C4 resin with 5 μ m diameter, 0.5 cm C18 resin with 3 μ m
595 diameter, and 29 cm of C18 resin with 1.8 μ m diameter. The column measured 30 cm in overall
596 length, with inner diameter of 100 μ m and outer diameter of 360 μ m. Electrospray ionization
597 was achieved at the source through application of 2,000 V of electricity through a T-connector at
598 the junction between the source, waste, and column capillaries. Spectra were acquired at the
599 MS1 level in data-dependent mode with scan range in the Orbitrap between 500 and 1200 m/z
600 and resolution of 60,000. Automatic gain control (AGC) was set to 2×10^5 with the maximum ion
601 inject time set to 100 ms. The Top N setting was used for subsequent fragment ion analysis, with
602 N=10. MS2 data collection was performed using the decision tree option, wherein ions with 2
603 charges were analyzed between 600-1200 m/z. Ions with 3-4 charges were analyzed between
604 500-1200 m/z. The lower ion intensity threshold was set to 5×10^4 , and selected ions were
605 isolated in the quadrupole at 0.5 Th. Fragmentation was performed using Collision-Induced
606 Dissociation, and ion detection and centroiding occurred in the linear ion trap with AGC rapid
607 scan rate of 1×10^4 . MS3 data was generated using synchronous precursor selection (58). No
608 more than 10 precursor ions were concurrently fragmented using High Energy Collisional
609 Dissociation fragmentation, and reporter ions were detected in the Orbitrap. The resolution was
610 set to 60,000 with lower threshold of 110 m/z. AGC of 1×10^5 was used here, with maximum
611 inject time of 100 ms. All data were collected in "centroid" mode.
612

613 **Proteomic data analysis**

614 Spectral data were analyzed using Proteome Discoverer 2.1. Spectral matching was performed
615 against a concatenated database of *Mus musculus* reference proteome appended to an HSV-1
616 reference proteome. SEQUEST-HT was used to match spectra against a target and decoy
617 database generated *in silico* (59). Precursor mass and fragment ion mass tolerances were set to
618 50 ppm and 0.6 Da, respectively. Trypsin was specified as the enzyme, with two missed
619 cleavages permitted. The length of accepted peptides was specified as 6 to 144 amino acids.
620 Oxidation of methionine residues was specified as a variable modification (+15.995 Da), and TMT
621 labeling at N-termini and on lysine residues (+229.163 Da) and carbamidomethylation of
622 cysteine residues (+57.021 Da) were specified as invariable modifications. False discovery rate of
623 1% was used to filter spectra at the peptide and protein level. Data were processed by filtering
624 peptide spectral matches (PSMs) to retain only high quality and low ambiguity spectra. Any
625 missing quantitation values within a 10-plex were replaced by a 1 to represent a baseline noise
626 value. PSMs with average quantitation values less than 10 or isolation interference greater than
627 25 were removed from the dataset. PSMs were summed at the protein level and raw values were
628 normalized against the median bridge channel value.

629

630 **Data and code availability**

631 Raw data for transcriptomics experiments were deposited as fastq files in the Sequence Read
632 Archives (SRA) under BioProject PRJNA553809. Raw data for HSV-1 timecourse proteomics
633 experiment can be found on ProteomeXchange under the identifier PXD014181. Hallmark
634 Interferon Alpha Response, GO NLRP3 Inflammasome Complex Assembly and GO Mitophagy
635 genesets were obtained from the publicly available GSEA/mSigDB collection at

636 <http://software.broadinstitute.org/gsea/msigdb/index.jsp>. Gene Expression Omnibus dataset
637 GSE34080 was accessed at <https://www.ncbi.nlm.nih.gov/geo>. There are no restrictions on raw
638 data, all requests can be addressed to the corresponding author.

639

640 **Statistics**

641 Statistical tests including unpaired t-test, Mann-Whitney, Wilcoxon signed-rank tests and two-
642 way ANOVA with correction for multiple comparisons were implemented in GraphPad Prism
643 and *R* where appropriate, as indicated in the figure legends. Details of statistical analysis method
644 and information including *n*, mean, and statistical significance values are indicated in the
645 corresponding sections of the main text, figure legends, or Methods. Experiments were
646 replicated three times unless otherwise specified. A *p* value of < 0.05 was considered to be
647 statistically significant. * $p < 0.05$, ** $p < 0.01$, *** $p < 0.001$, **** $p < 0.0001$; ns, not significant.

648

649 **Study approval**

650 All animal care and procedures were performed in accordance with the institutional and NIH
651 guidelines, and approved by the Animal Care Committee at University of Illinois at Chicago (ACC
652 protocols 17-077 and 20-065).

653

654 **Acknowledgments**

655 This work was supported by NIH grants R01EY024710 (DS), R01EY029426 (DS), R01AI139768
656 (DS), R21AI128171 (DS), R21AI133557 (DS), NIH fellowship F30EY025981 (AA), and
657 departmental core grant P30EY001792 (DS). We are grateful to Ruth Zhelka and Tara Nguyen
658 for assistance with departmental imaging and animal facilities.

659

660 **Author contributions**

661 Conceptualization, A.A. and D.S.; Methodology, A.A., B.A.T., R.K.S., T.Y., D.J., J.A., J.H., L.K., C.D.P.,
662 S.R.H., E.J.K., A.C., J.M.W., D.J.G., I.V., J-P.L., D.L.P., P.W.F., D.S.; Software, A.A., B.A.T., A.C., J.M.W.;
663 Validation, A.A., B.A.T., R.K.S., T.Y., D.J., J.A., J.H., L.K., C.D.P., S.R.H., E.J.K., A.C., J.M.W.; Formal
664 Analysis, A.A., B.A.T., A.C., J.M.W.; Investigation, A.A., B.A.T., R.K.S., T.Y., D.J., J.A., J.H., L.K., C.D.P.,
665 S.R.H., E.J.K., A.C., J.M.W.; Resources, A.A., B.A.T., A.C., J.M.W., I.V., J-P.L. D.J.G., P.W.F., D.L.P., D.S.;
666 Data Curation, A.A., B.A.T., A.C., J.M.W.; Writing – Original Draft, A.A.; Writing – Review and
667 Editing, A.A., B.A.T., R.K.S., T.Y., D.J., J.A., J.H., L.K., C.D.P., S.R.H., E.J.K., A.C., J.M.W., D.J.G., I.V., J-
668 P.L., D.L.P., P.W.F., D.S.; Visualization, A.A. and B.A.T.; Supervision, A.A., P.W.F., D.L.P., D.J.G, D.S.;
669 Funding Acquisition, A.A. and D.S.

670

671 **Conflict of interest statement**

672 The authors have declared that no conflict of interest exists.

References

1. Vlodavsky I, Ilan N, and Sanderson RD. Forty Years of Basic and Translational Heparanase Research. *Adv Exp Med Biol.* 2020;1221(3-59).
2. Vlodavsky I, Gross-Cohen M, Weissmann M, Ilan N, and Sanderson RD. Opposing Functions of Heparanase-1 and Heparanase-2 in Cancer Progression. *Trends Biochem Sci.* 2018;43(1):18-31.
3. Kundu S, Xiong A, Spyrou A, Wicher G, Marinescu VD, Edqvist PD, Zhang L, Essand M, Dimberg A, Smits A, et al. Heparanase Promotes Glioma Progression and Is Inversely Correlated with Patient Survival. *Mol Cancer Res.* 2016;14(12):1243-53.
4. Jung O, Trapp-Stamborski V, Purushothaman A, Jin H, Wang H, Sanderson RD, and Rapraeger AC. Heparanase-induced shedding of syndecan-1/CD138 in myeloma and endothelial cells activates VEGFR2 and an invasive phenotype: prevention by novel synstatins. *Oncogenesis.* 2016;5(e202).
5. He YQ, Sutcliffe EL, Bunting KL, Li J, Goodall KJ, Poon IK, Hulett MD, Freeman C, Zafar A, McInnes RL, et al. The endoglycosidase heparanase enters the nucleus of T lymphocytes and modulates H3 methylation at actively transcribed genes via the interplay with key chromatin modifying enzymes. *Transcription.* 2012;3(3):130-45.
6. Yang Y, Gorzelanny C, Bauer AT, Halter N, Komljenovic D, Bauerle T, Borsig L, Roblek M, and Schneider SW. Nuclear heparanase-1 activity suppresses melanoma progression via its DNA-binding affinity. *Oncogene.* 2015;34(47):5832-42.
7. Hadigal SR, Agelidis AM, Karasneh GA, Antoine TE, Yakoub AM, Ramani VC, Djalilian AR, Sanderson RD, and Shukla D. Heparanase is a host enzyme required for herpes simplex virus-1 release from cells. *Nat Commun.* 2015;6(6985).
8. Puerta-Guardo H, Glasner DR, and Harris E. Dengue Virus NS1 Disrupts the Endothelial Glycocalyx, Leading to Hyperpermeability. *PLoS Pathog.* 2016;12(7):e1005738.
9. Guo C, Zhu Z, Guo Y, Wang X, Yu P, Xiao S, Chen Y, Cao Y, and Liu X. Heparanase Upregulation Contributes to Porcine Reproductive and Respiratory Syndrome Virus Release. *J Virol.* 2017;91(15).
10. Agelidis A, and Shukla D. Heparanase, Heparan Sulfate and Viral Infection. *Adv Exp Med Biol.* 2020;1221(759-70).
11. Agelidis AM, Hadigal SR, Jaishankar D, and Shukla D. Viral Activation of Heparanase Drives Pathogenesis of Herpes Simplex Virus-1. *Cell Rep.* 2017;20(2):439-50.
12. Hong X, Nelson K, Lemke N, and Kalkanis SN. Heparanase expression is associated with histone modifications in glioblastoma. *Int J Oncol.* 2012;40(2):494-500.

13. Nobuhisa T, Naomoto Y, Okawa T, Takaoka M, Gunduz M, Motoki T, Nagatsuka H, Tsujigiwa H, Shirakawa Y, Yamatsuji T, et al. Translocation of heparanase into nucleus results in cell differentiation. *Cancer Sci.* 2007;98(4):535-40.
14. Schubert SY, Ilan N, Shushy M, Ben-Izhak O, Vlodaysky I, and Goldshmidt O. Human heparanase nuclear localization and enzymatic activity. *Lab Invest.* 2004;84(5):535-44.
15. van der Maaten L, and Hinton G. Visualizing Data using t-SNE. *Journal of Machine Learning Research.* 2008;9(2579-605).
16. Bodenhofer U, Kothmeier A, and Hochreiter S. APCluster: an R package for affinity propagation clustering. *Bioinformatics.* 2011;27(17):2463-4.
17. Schneider WM, Chevillotte MD, and Rice CM. Interferon-stimulated genes: a complex web of host defenses. *Annu Rev Immunol.* 2014;32(513-45).
18. Perng YC, and Lenschow DJ. ISG15 in antiviral immunity and beyond. *Nat Rev Microbiol.* 2018;16(7):423-39.
19. Sacks WR, and Schaffer PA. Deletion mutants in the gene encoding the herpes simplex virus type 1 immediate-early protein ICP0 exhibit impaired growth in cell culture. *J Virol.* 1987;61(3):829-39.
20. Smith MC, Boutell C, and Davido DJ. HSV-1 ICP0: paving the way for viral replication. *Future Virol.* 2011;6(4):421-9.
21. Gu H, Poon AP, and Roizman B. During its nuclear phase the multifunctional regulatory protein ICP0 undergoes proteolytic cleavage characteristic of polyproteins. *Proc Natl Acad Sci U S A.* 2009;106(45):19132-7.
22. Zcharia E, Jia J, Zhang X, Baraz L, Lindahl U, Peretz T, Vlodaysky I, and Li JP. Newly generated heparanase knock-out mice unravel co-regulation of heparanase and matrix metalloproteinases. *PLoS One.* 2009;4(4):e5181.
23. Lobo AM, Agelidis AM, and Shukla D. Pathogenesis of herpes simplex keratitis: The host cell response and ocular surface sequelae to infection and inflammation. *Ocul Surf.* 2019;17(1):40-9.
24. Rowe AM, St Leger AJ, Jeon S, Dhaliwal DK, Knickelbein JE, and Hendricks RL. Herpes keratitis. *Prog Retin Eye Res.* 2013;32(88-101).
25. Maelfait J, Liverpool L, Bridgeman A, Ragan KB, Upton JW, and Rehwinkel J. Sensing of viral and endogenous RNA by ZBP1/DAI induces necroptosis. *EMBO J.* 2017;36(17):2529-43.
26. McComb S, Cessford E, Alturki NA, Joseph J, Shutinoski B, Startek JB, Gamero AM, Mossman KL, and Sad S. Type-I interferon signaling through ISGF3 complex is required

- for sustained Rip3 activation and necroptosis in macrophages. *Proc Natl Acad Sci U S A*. 2014;111(31):E3206-13.
27. Thapa RJ, Nogusa S, Chen P, Maki JL, Lerro A, Andrade M, Rall GF, Degterev A, and Balachandran S. Interferon-induced RIP1/RIP3-mediated necrosis requires PKR and is licensed by FADD and caspases. *Proc Natl Acad Sci U S A*. 2013;110(33):E3109-18.
 28. Honda K, Takaoka A, and Taniguchi T. Type I interferon [corrected] gene induction by the interferon regulatory factor family of transcription factors. *Immunity*. 2006;25(3):349-60.
 29. Yoneyama M, Suhara W, Fukuhara Y, Fukuda M, Nishida E, and Fujita T. Direct triggering of the type I interferon system by virus infection: activation of a transcription factor complex containing IRF-3 and CBP/p300. *EMBO J*. 1998;17(4):1087-95.
 30. de Mestre AM, Rao S, Hornby JR, Soe-Htwe T, Khachigian LM, and Hulett MD. Early growth response gene 1 (EGR1) regulates heparanase gene transcription in tumor cells. *J Biol Chem*. 2005;280(42):35136-47.
 31. Jiao W, Chen Y, Song H, Li D, Mei H, Yang F, Fang E, Wang X, Huang K, Zheng L, et al. HPSE enhancer RNA promotes cancer progression through driving chromatin looping and regulating hnRNPU/p300/EGR1/HPSE axis. *Oncogene*. 2018;37(20):2728-45.
 32. Baer A, Lundberg L, Swales D, Waybright N, Pinkham C, Dinman JD, Jacobs JL, and Kehn-Hall K. Venezuelan Equine Encephalitis Virus Induces Apoptosis through the Unfolded Protein Response Activation of EGR1. *J Virol*. 2016;90(7):3558-72.
 33. Zhu Z, Du X, Li P, Zhang X, Yang F, Cao W, Tian H, Zhang K, Liu X, and Zheng H. Early Growth Response Gene-1 Suppresses Foot-and-Mouth Disease Virus Replication by Enhancing Type I Interferon Pathway Signal Transduction. *Front Microbiol*. 2018;9(2326).
 34. Kim S-J, and Lee S-M. Necrostatin-1 Protects Against d-Galactosamine and Lipopolysaccharide-Induced Hepatic Injury by Preventing TLR4 and RAGE Signaling. *Inflammation*. 2017;40(6):1912-23.
 35. Bhattacharjee A, Mulya A, Pal S, Roy B, Feldman GM, and Cathcart MK. Monocyte 15-lipoxygenase gene expression requires ERK1/2 MAPK activity. *J Immunol*. 2010;185(9):5211-24.
 36. Chen SH, Yao HW, Chen IT, Shieh B, Li C, and Chen SH. Suppression of transcription factor early growth response 1 reduces herpes simplex virus lethality in mice. *J Clin Invest*. 2008;118(10):3470-7.
 37. Yao HW, Chen SH, Li C, Tung YY, and Chen SH. Suppression of transcription factor early growth response 1 reduces herpes simplex virus 1-induced corneal disease in mice. *J Virol*. 2012;86(16):8559-67.

38. Hur EM, and Zhou FQ. GSK3 signalling in neural development. *Nat Rev Neurosci*. 2010;11(8):539-51.
39. Bidwell BN, Slaney CY, Withana NP, Forster S, Cao Y, Loi S, Andrews D, Mikeska T, Mangan NE, Samarajiwa SA, et al. Silencing of Irf7 pathways in breast cancer cells promotes bone metastasis through immune escape. *Nat Med*. 2012;18(8):1224-31.
40. Zhao Y, Chen W, Zhu W, Meng H, Chen J, and Zhang J. Overexpression of Interferon Regulatory Factor 7 (IRF7) Reduces Bone Metastasis of Prostate Cancer Cells in Mice. *Oncol Res*. 2017;25(4):511-22.
41. Mayr B, and Montminy M. Transcriptional regulation by the phosphorylation-dependent factor CREB. *Nat Rev Mol Cell Biol*. 2001;2(8):599-609.
42. Carlezon WA, Jr., Duman RS, and Nestler EJ. The many faces of CREB. *Trends Neurosci*. 2005;28(8):436-45.
43. Dyson HJ, and Wright PE. Role of Intrinsic Protein Disorder in the Function and Interactions of the Transcriptional Coactivators CREB-binding Protein (CBP) and p300. *J Biol Chem*. 2016;291(13):6714-22.
44. Gantner BN, Jin H, Qian F, Hay N, He B, and Ye RD. The Akt1 isoform is required for optimal IFN-beta transcription through direct phosphorylation of beta-catenin. *J Immunol*. 2012;189(6):3104-11.
45. Zhu L, and Jones C. The canonical Wnt/beta-catenin signaling pathway stimulates herpes simplex virus 1 productive infection. *Virus Res*. 2018;256(29-37).
46. Zvezdaryk KJ, Combs JA, Morris CA, and Sullivan DE. Regulation of Wnt/beta-catenin signaling by herpesviruses. *World J Virol*. 2016;5(4):144-54.
47. Tokunaga Y, Osawa Y, Ohtsuki T, Hayashi Y, Yamaji K, Yamane D, Hara M, Munekata K, Tsukiyama-Kohara K, Hishima T, et al. Selective inhibitor of Wnt/beta-catenin/CBP signaling ameliorates hepatitis C virus-induced liver fibrosis in mouse model. *Sci Rep*. 2017;7(1):325.
48. Desai P, and Person S. Incorporation of the green fluorescent protein into the herpes simplex virus type 1 capsid. *J Virol*. 1998;72(9):7563-8.
49. Montgomery RI, Warner MS, Lum BJ, and Spear PG. Herpes simplex virus-1 entry into cells mediated by a novel member of the TNF/NGF receptor family. *Cell*. 1996;87(3):427-36.
50. Shukla D, Rowe CL, Dong Y, Racaniello VR, and Spear PG. The murine homolog (Mph) of human herpesvirus entry protein B (HveB) mediates entry of pseudorabies virus but not herpes simplex virus types 1 and 2. *J Virol*. 1999;73(5):4493-7.

51. Fux L, Feibish N, Cohen-Kaplan V, Gingis-Velitski S, Feld S, Geffen C, Vlodayvsky I, and Ilan N. Structure-function approach identifies a COOH-terminal domain that mediates heparanase signaling. *Cancer Res.* 2009;69(5):1758-67.
52. Roeder HG, Manke T, O'Keeffe S, Vingron M, and Haas SA. PASTAA: identifying transcription factors associated with sets of co-regulated genes. *Bioinformatics.* 2009;25(4):435-42.
53. Metwally AA, Yang J, Ascoli C, Dai Y, Finn PW, and Perkins DL. MetaLonDA: a flexible R package for identifying time intervals of differentially abundant features in metagenomic longitudinal studies. *Microbiome.* 2018;6(1):32.
54. Bindea G, Mlecnik B, Hackl H, Charoentong P, Tosolini M, Kirilovsky A, Fridman WH, Pages F, Trajanoski Z, and Galon J. ClueGO: a Cytoscape plug-in to decipher functionally grouped gene ontology and pathway annotation networks. *Bioinformatics.* 2009;25(8):1091-3.
55. Yu G, Wang LG, Han Y, and He QY. clusterProfiler: an R package for comparing biological themes among gene clusters. *OMICS.* 2012;16(5):284-7.
56. Lapek JD, Jr., Lewinski MK, Wozniak JM, Guatelli J, and Gonzalez DJ. Quantitative Temporal Viromics of an Inducible HIV-1 Model Yields Insight to Global Host Targets and Phospho-Dynamics Associated with Protein Vpr. *Mol Cell Proteomics.* 2017;16(8):1447-61.
57. Wang Y, Yang F, Gritsenko MA, Wang Y, Clauss T, Liu T, Shen Y, Monroe ME, Lopez-Ferrer D, Reno T, et al. Reversed-phase chromatography with multiple fraction concatenation strategy for proteome profiling of human MCF10A cells. *Proteomics.* 2011;11(10):2019-26.
58. Ting L, Rad R, Gygi SP, and Haas W. MS3 eliminates ratio distortion in isobaric multiplexed quantitative proteomics. *Nat Methods.* 2011;8(11):937-40.
59. Elias JE, and Gygi SP. Target-decoy search strategy for increased confidence in large-scale protein identifications by mass spectrometry. *Nat Methods.* 2007;4(3):207-14.

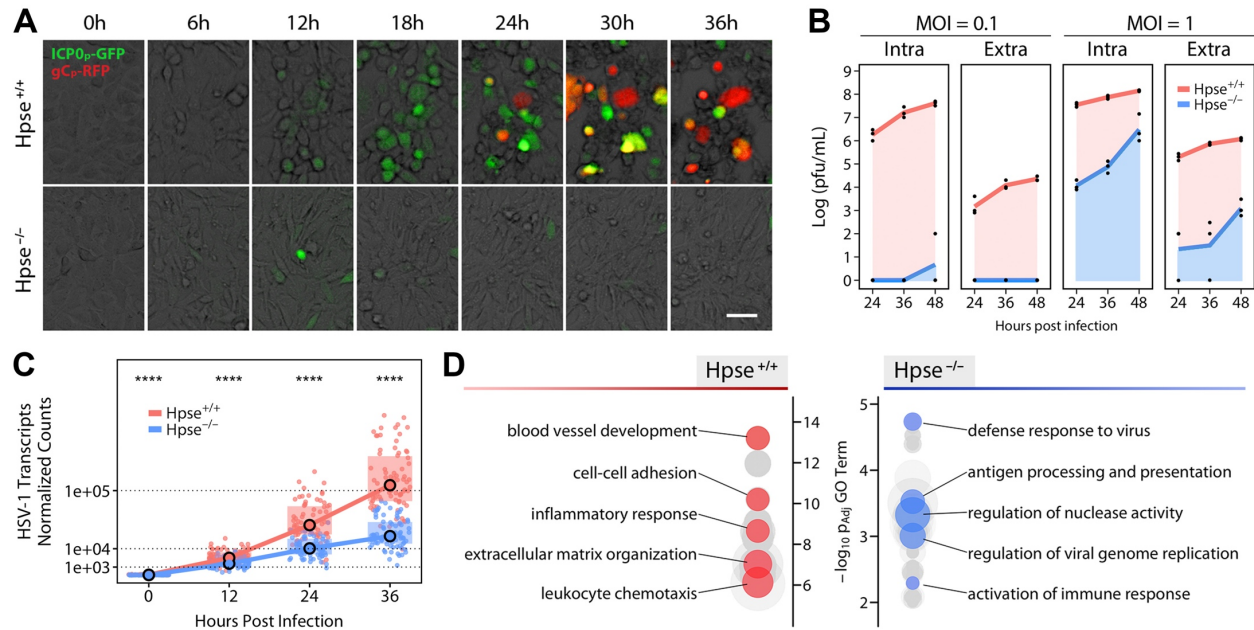


Figure 1 | Baseline differences in host gene expression grant HPSE-deficient cells resistance to viral infection.

(A) Representative images of infection timecourse of wildtype ($Hpse^{+/+}$) and heparanase-deficient ($Hpse^{-/-}$) mouse embryonic fibroblasts (MEFs) with a dual fluorescence strain of HSV-1. Green signal indicates viral immediate early gene expression (ICP0) while red signal indicates viral late gene expression (gC). Scale bar, 50 μ m.

(B) Titers of intracellular (Intra) and extracellular (Extra) HSV-1 detected at two multiplicities of infection (MOI) in wildtype and $Hpse^{-/-}$ MEFs ($n=3$).

(C) HSV-1 viral gene expression as quantified by transcriptomics analysis. Each data point represents one of 74 detected viral transcripts. Median and interquartile range are plotted, significance analyzed by Wilcoxon signed-rank test.

(D) Baseline differential enrichment of gene ontology terms of $Hpse^{+/+}$ and $Hpse^{-/-}$ cells in the absence of infection. Each node represents a unique term, with node size representing fold enrichment. Select summary terms are highlighted.

**** $p < 0.0001$.

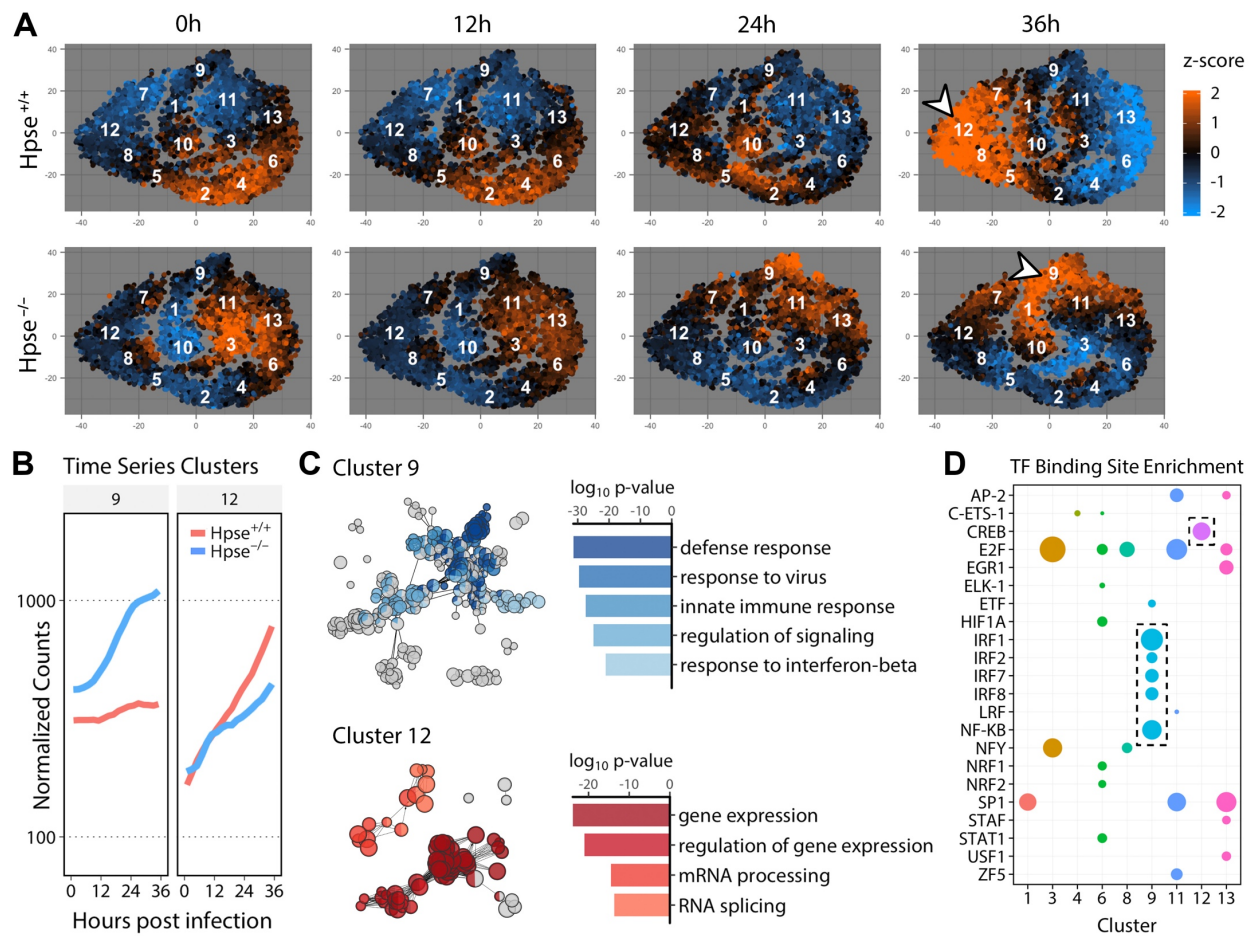


Figure 2 | Temporal viromics catalogs shifts in transcriptional landscape and reveals functional clusters of genes dependent on HPSE.

(A) t-stochastic neighbor embedding (t-SNE) projection depicting relative expression of differentially expressed genes, with clustering based on expression patterns over infection timecourse. Centroids of each of 13 clusters are labelled with respective identifier. Arrowheads indicate clusters further dissected below.

(B) Median gene expression of selected clusters displayed over time.

(C) Representation of significantly enriched gene ontology (GO) terms performed with ClueGO. Node sizes relative to GO term enrichment, with functionally related terms grouped by color and indicated by corresponding bar plot.

(D) Significant transcription factor binding site enrichment analysis represented by cluster, with bubble sizes relative to enrichment score.

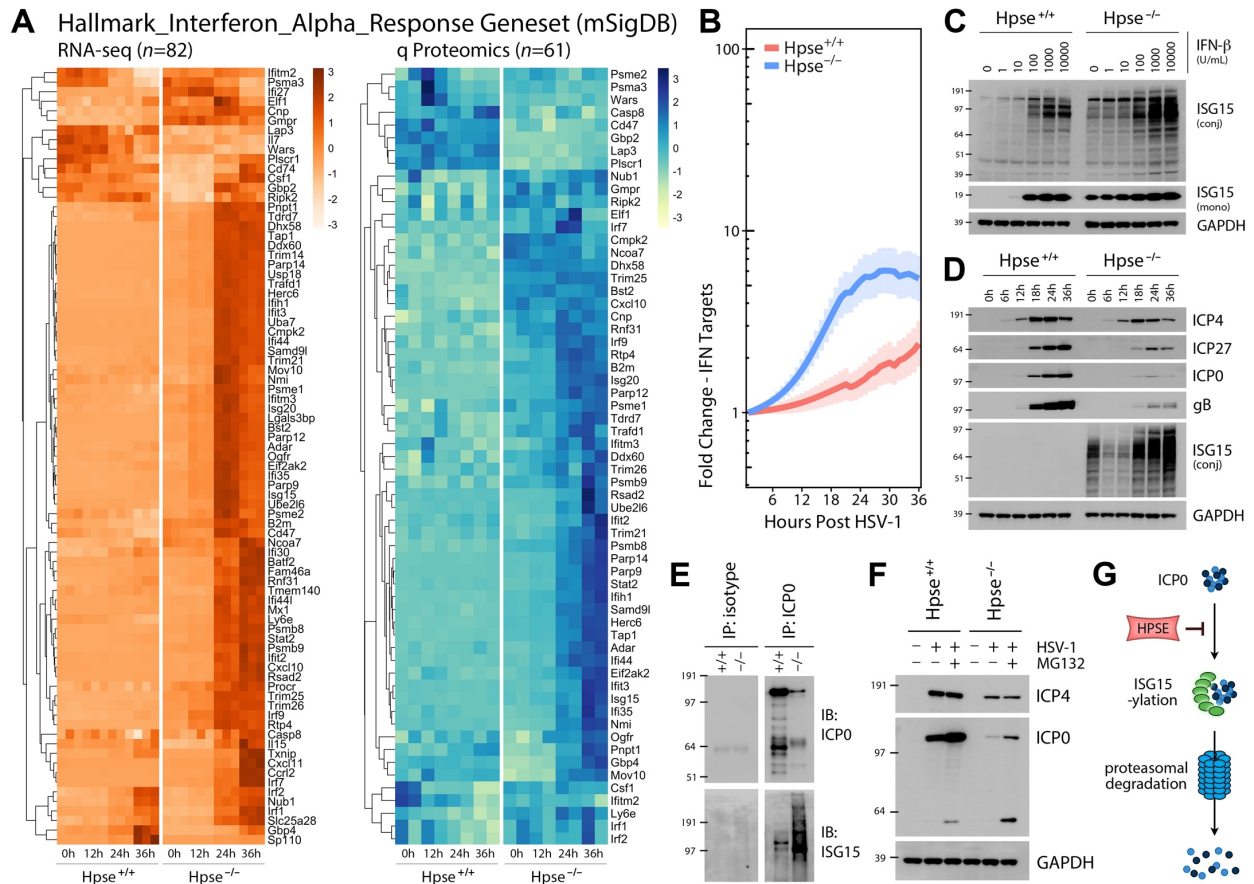


Figure 3 | HPSE restricts type I interferon response and drives virus production through inhibition of degradation of immediate early protein ICP0.

(A) Transcriptomic and proteomic datasets filtered based on Hallmark_Interferon_Alpha_Response geneset ($n=91$ genes) obtained from mSigDb.

(B) Transcript expression of Hallmark_Interferon_Alpha_Response subset displayed as fold change over baseline, with bolded lines signifying mean expression and shaded areas indicating standard error. Splines generated using MetaLonDA.

(C) Increased type I interferon sensitivity in *Hpse*^{-/-} cells at baseline and with interferon (IFN)- β administration for 18 h, exemplified by expression of interferon stimulated gene (ISG)15 monomer and protein-conjugated forms.

(D) Representative western blot analysis of cell lysates from wildtype and *Hpse*^{-/-} MEFs indicating selective defect in viral protein production in HPSE deficiency. gB is a late (γ) gene, while ICP4, ICP27, and ICP0 are immediate early (α) genes.

(E) Western blot analysis of cell lysate, isotype immunoprecipitation (IP), ICP0 IP of wildtype and *Hpse*^{-/-} cells after 24 h HSV-1 infection, with 10 μ M MG132 added for the final 4 h.

(F) Immediate early viral protein expression in the presence of proteasome inhibitor MG132 (10 μ M for last 4 h of 24 h infection) shown by western blot analysis of cell lysates.

(G) Proposed model depicting ability of HPSE to interfere with ISG15 conjugation and proteasomal degradation of viral ICP0.

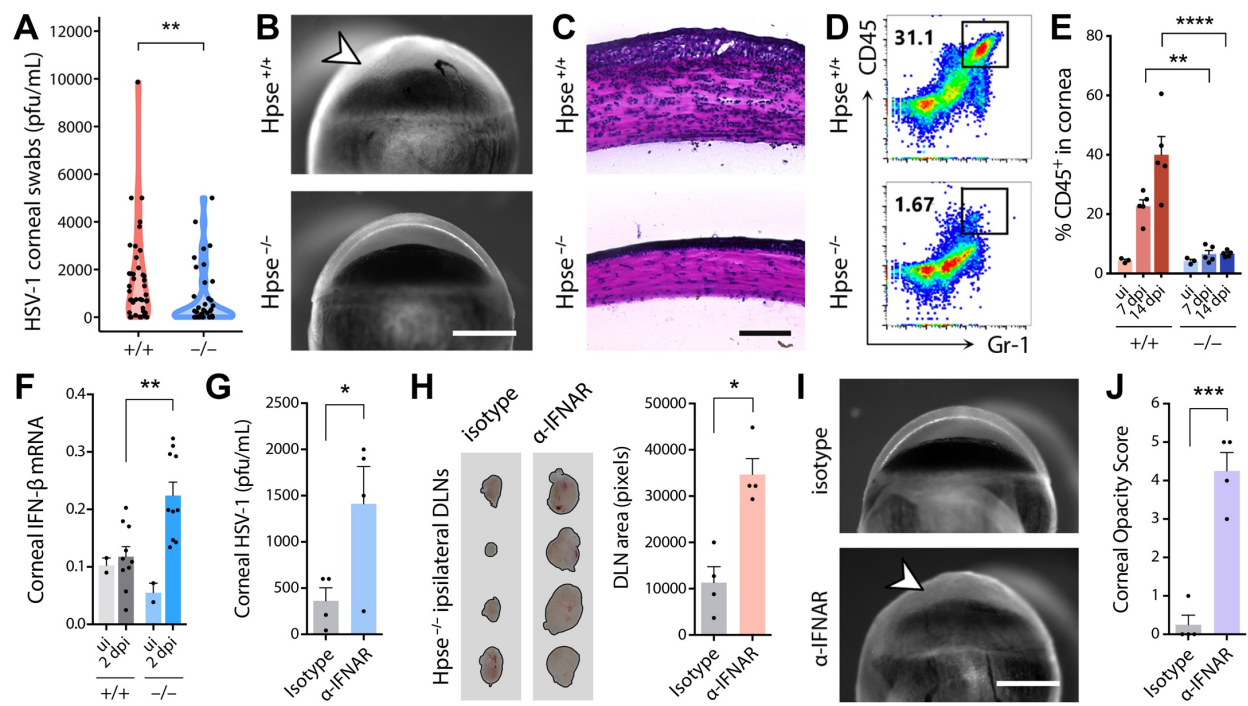


Figure 4 | Deletion of HPSE protects from cellular infiltration and associated inflammation in a murine model of corneal infection.

(A) HSV-1 titers 2 d following corneal infection of *Hpse*^{+/+} and *Hpse*^{-/-} mice ($n=44$). Significance determined by Wilcoxon signed-rank test.

(B-D) Markedly decreased corneal inflammation and infiltration (arrowhead) in *Hpse*-deficient mice 14 d following HSV-1 infection observed by gross imaging (B), hematoxylin-eosin histology (C), and flow cytometry of dissociated corneal tissues (D). Scale bar (B), 1 mm; scale bar (C), 50 μ m.

(E) Quantification of leukocytes (CD45⁺) present in corneal tissue at indicated day post infection (dpi) as observed by flow cytometry ($n=5$ for infected animals, $n=3$ for uninfected animals). Significance determined by two-way ANOVA with Sidak correction for multiple comparisons.

(F) Corneal IFN- β mRNA copy number relative to β -actin measured at 2 dpi ($n=10$). Uninfected (ui) samples constituted 2 pools of 5 mouse corneas each. Significance determined by two-way ANOVA with Sidak correction for multiple comparisons.

(G-J) Partial restoration of viral titers and cellular infiltration in HPSE-deficient mice after topical application of α -IFNAR monoclonal antibody, observed by ocular wash titers (G), gross analysis of ipsilateral draining lymph nodes (DLN) (H) and gross analysis (I) and scoring (J) of corneal opacity ($n=4$). Scale bar, 1 mm.

Data represent mean \pm SEM. Significance determined by unpaired t-test unless otherwise specified. * $p<0.05$, ** $p<0.01$, *** $p<0.001$, **** $p<0.0001$.

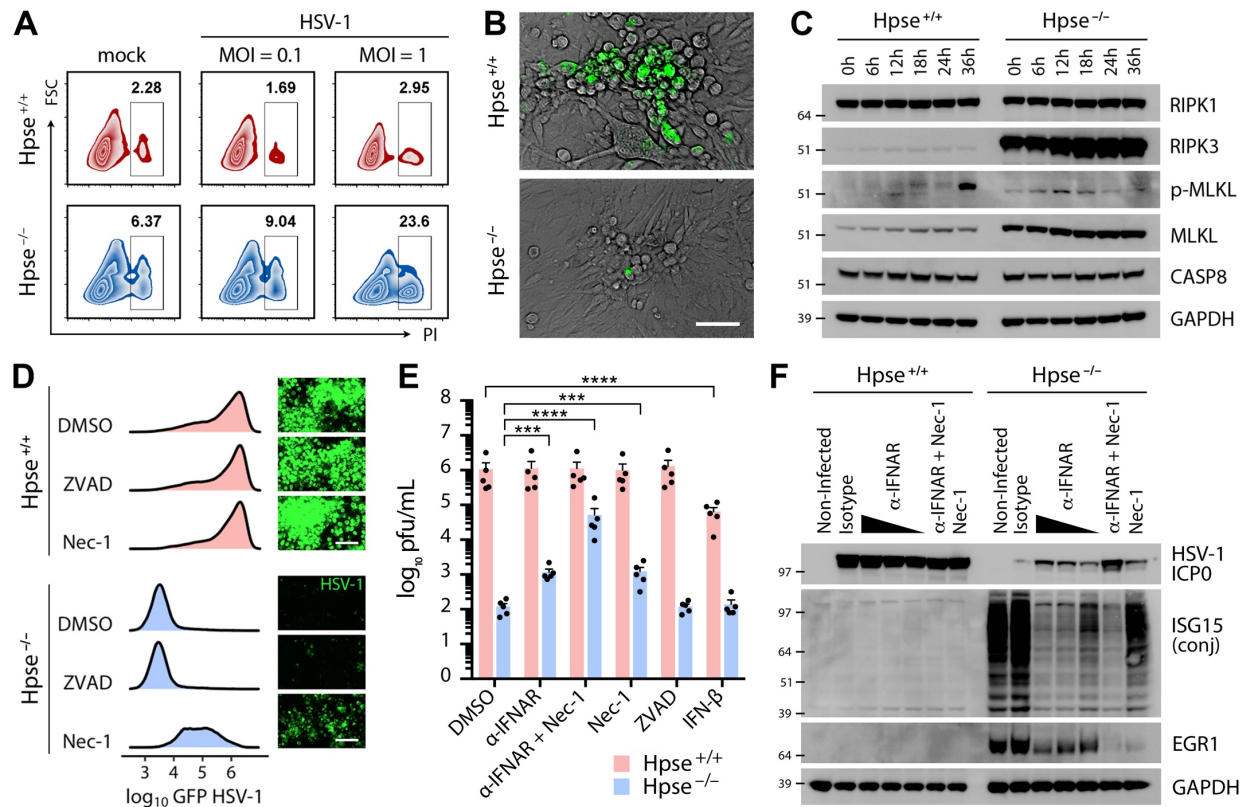


Figure 5 | Attenuation of interferon response and necroptotic cell death restores infection in the absence of HPSE.

(A) Measurement of cell death by flow cytometry detection of propidium iodide (PI) cellular uptake after 24 h HSV-1 or mock infection.

(B) Immunofluorescence microscopy of cells infected with GFP-HSV-1, images captured at 24 hpi. Despite profound abrogation of virus production in absence of HPSE, multiple clusters of rounded and detached cells resembling plaques are observed after infection. Scale bar, 50 μ m.

(C) Western blot analysis of key proteins involved in induction of necroptosis at indicated times post infection.

(D) Representative flow cytometry quantification and micrographs of Hpse^{+/+} and Hpse^{-/-} cells after infection with GFP-HSV-1 for 48 h, incubated with inhibitors of apoptosis (ZVAD) or necroptosis (Nec-1) as indicated. Scale bar, 100 μ m.

(E) Restoration of virus production in Hpse^{-/-} cells with blocking of interferon alpha receptor (α -IFNAR) and necroptosis (Nec-1) showing a synergistic effect ($n=5$).

(F) Inverse relationship between viral infected cell protein (ICP0) and ISG15 expression demonstrated by western blot, with near complete rescue of virus production observed upon α -IFNAR and Nec-1 treatment in Hpse^{-/-} cells.

Data represent mean \pm SEM. Significance determined by two-way ANOVA with Dunnett correction for multiple comparisons against control (DMSO). *** $p < 0.001$, **** $p < 0.0001$.

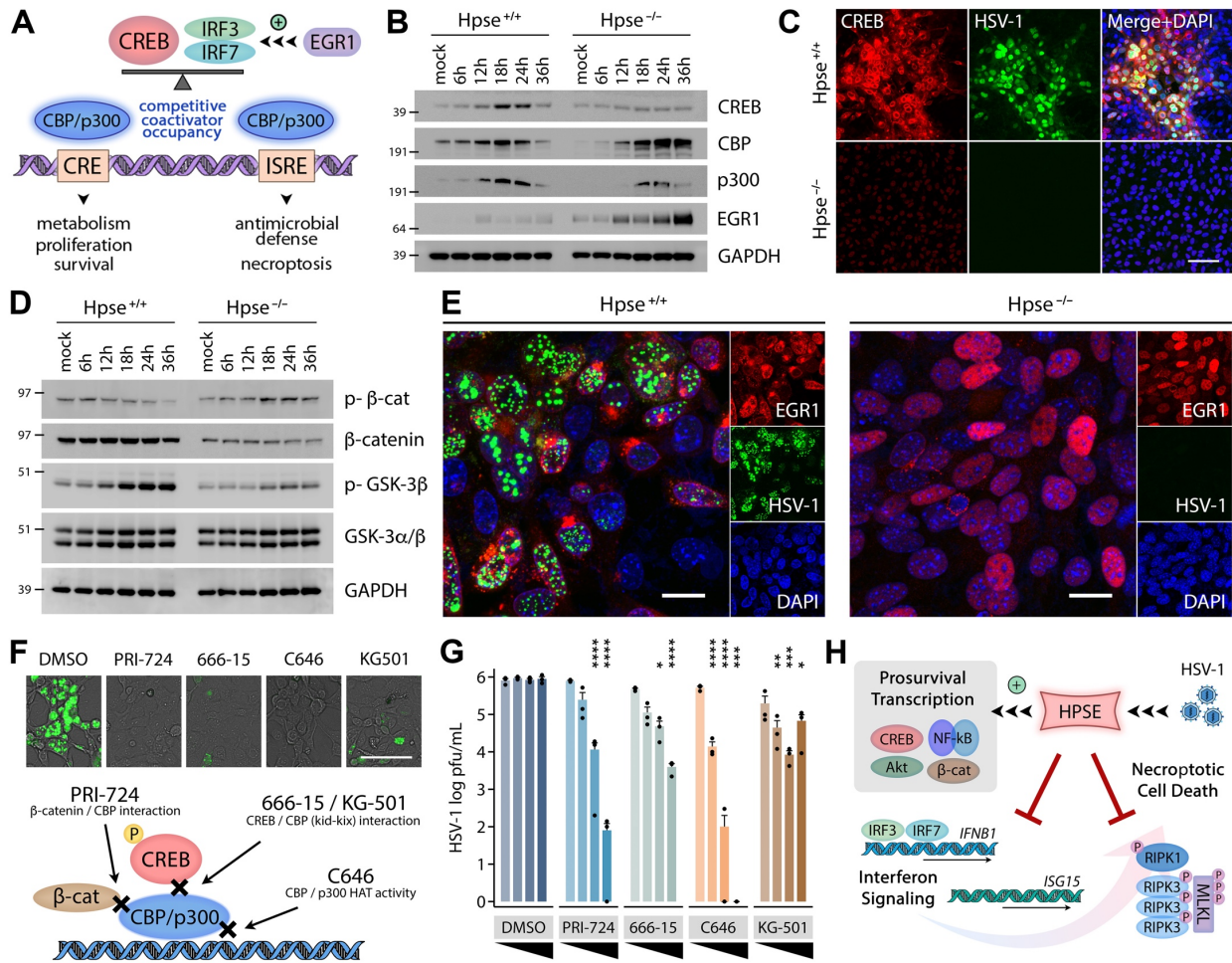


Figure 6 | Bioinformatics-guided analysis of transcription factor activation in viral infection identifies potent antiviral compounds.

(A) Schematic depicting CREB and IRF competitive binding for CBP/p300 transcriptional coactivators, based on published literature.

(B) Representative western blot analysis of CREB signaling induction with infection of wildtype and Hpse-KO cells.

(C) Confocal immunofluorescence microscopy of wildtype and Hpse-KO cells showing CREB upregulation in infected wildtype cells. Scale bar, 100 μ m.

(D) Representative western blot analysis of β -catenin signaling induction with infection of wildtype and Hpse-KO cells.

(E) Confocal immunofluorescence microscopy of wildtype and Hpse-KO cells showing EGR1 cellular localization and GFP-HSV-1. Scale bar, 20 μ m.

(F) *Top*, Representative immunofluorescence micrographs of human corneal epithelial cells infected with GFP-HSV-1 and then incubated with specified inhibitors at 2 h post GFP-HSV-1 infection, images captured at 24 hpi. Scale bar, 100 μ m. *Bottom*, Schematic depicting known mechanisms of action of selected inhibitors.

(G) Viral titers obtained from human corneal epithelial cells after incubation of specified inhibitors at concentrations 12.5, 25, 50 and 100 μM . (666-15 was used at concentrations of 5, 10, 15, and 20 μM due to unacceptable toxicity at higher levels). Significance determined by two-way ANOVA with Dunnett correction for multiple comparisons against control (DMSO) at respective concentration ($n=3$).

(H) Model of HPSE function at the interface of innate defense responses and cell survival. Infection and other cellular insults trigger activation of multiple prosurvival factors, including CREB, Akt, NF- κB and β -catenin. Previous work and this study show that HPSE modulates nuclear trafficking of these TFs, which drive cellular proliferation, microbial replication and carcinogenesis. Here we show that HPSE inhibits type I interferon production and induction of necroptosis. These innate stress responses likely act to protect multicellular tissues from viral or cancerous spread by preventing uncontrolled cellular proliferation.